

RESEARCH ARTICLE

WILEY

Using an autonomous underwater vehicle with onboard stochastic advection-diffusion models to map excursion sets of environmental variables

Karine Hagesæther Foss¹ | Gunhild Elisabeth Berget^{2,3}  | Jo Eidsvik¹

¹Department of Mathematical Sciences, Norwegian University of Science and Technology, Trondheim, Norway

²Department of Engineering Cybernetics, Norwegian University of Science and Technology, Trondheim, Norway

³Centre of Autonomous Marine Operations and Systems (AMOS), Trondheim, Norway

Correspondence

Gunhild Elisabeth Berget, Department of Engineering Cybernetics, Norwegian University of Science and Technology, Trondheim, Norway.
Email: gunhild.berget@ntnu.no

Funding information

Norges Forskningsråd, Grant/Award Numbers: 223254, 267793, 305445

Abstract

New robotic sensor platforms have computing resources that enable a rich set of tasks for adaptive monitoring of the environment. But to substantially augment the toolbox of environmental sensing, such platforms must be embedded with realistic statistical models and coherent methodologies for designing experiments and assimilating the data. In this article, we develop myopic and hybrid strategies for autonomous underwater vehicle sampling in space and time. These strategies are based on a stochastic advection-diffusion Gaussian process model for the mine tailings concentration in a Norwegian fjord, and the goal is to monitor the excursion set (ES) of high concentrations. Closed form expressions for the expected misclassification probabilities of the ES enable real-time operation on board the autonomous vehicle, and this is used to guide the spatio-temporal sampling. Simulation studies show that the suggested strategies outperform other approaches that either (i) simplify the models for spatio-temporal variation, or (ii) simplify the design criterion. A field test shows how autonomous underwater sampling is useful for refining an initial stochastic advection-diffusion model. These experiments further show that the vehicle can adapt to focus on regions with intermediate concentrations where it is natural to improve the ES prediction.

KEYWORDS

autonomous underwater vehicle, excursion sets, oceanography, sampling design, spatio-temporal statistics, stochastic advection-diffusion model

1 | INTRODUCTION

There has recently been increased focus on the environmental impacts of human activities on oceans and coastal areas. For example, oil spills have big consequences for life along the coast, and plastic waste has proved to be extremely harmful for sea life. In this article, we consider the disposal of mining waste in fjords, which has caused controversy between environmental activists, aquacultural industries, and mining companies. The case study is from Frønfjorden (Figure 1), which is one of five active mining seafills in Norway. When mine tailings are deposited in a fjord, it is important that the contamination is monitored to predict with reasonable certainty that the environmental damage is below a critical level. Various tools can be used to monitor the concentration in space and time. With the advent of new sensors and

This is an open access article under the terms of the Creative Commons Attribution-NonCommercial-NoDerivs License, which permits use and distribution in any medium, provided the original work is properly cited, the use is non-commercial and no modifications or adaptations are made.

© 2021 The Authors. *Environmetrics* published by John Wiley & Sons, Ltd.

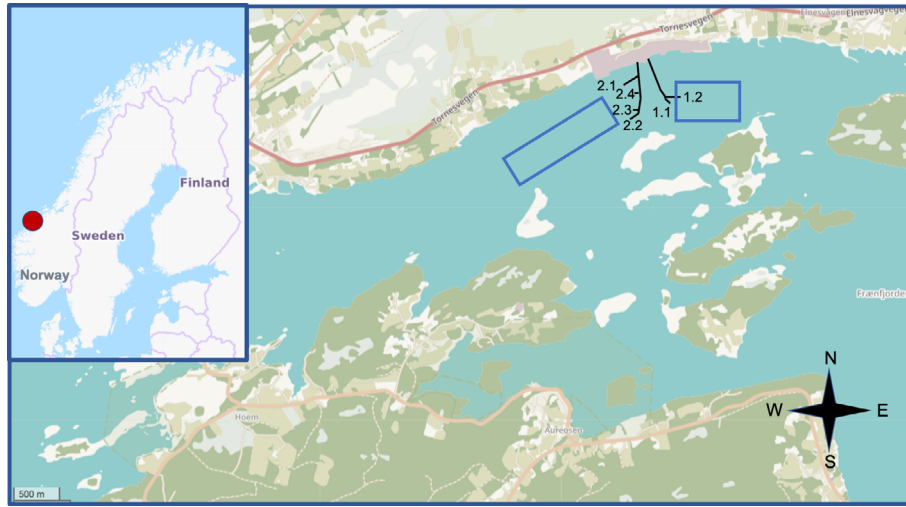


FIGURE 1 Position of mining seafill in Frænfjorden, Norway. The rectangles show the two domains used for, respectively, the simulation study (east side) and the field experiments (west side). The numbered pipes indicate the possible outlets where mine tailings are deposited

robotic vehicles such as autonomous underwater vehicles (AUVs), new monitoring opportunities have emerged. AUVs have become less expensive and more robust, and they can now be used for adaptive scientific sampling in the harsh oceans (Fossum et al., 2018).

The monitoring of contaminants must build on a criterion, and we here focus on the mapping of spatial regions where the concentration is above a specified critical threshold at the end-time of the considered monitoring interval. The resulting spatial subdomain with concentrations above the threshold limit is called an excursion set (ES). The design criterion for effective monitoring is based on minimizing the expected misclassification probabilities associated with the ES. There has recently been interest in studying ESs for environmental applications: French and Sain (2013) explore extreme precipitation. Bolin and Lindgren (2015) show an application with air pollution exceeding the limits set by the European Union. Sommerfeld et al. (2018) use ESs to study temperature changes.

To enable onboard data assimilation and evaluation of sampling designs, a low-complexity spatio-temporal stochastic model is needed to represent the dynamical variables. In this article, we focus on spatio-temporal Gaussian process (GP) models, see, for example, Cressie and Wikle (2011), that can act as an emulator or surrogate model (Gramacy, 2020) for more complex and computer intensive ocean models. Specifically, we construct this GP by using an advection-diffusion stochastic partial differential equation (SPDE) (Sigrist et al., 2015b). Within these modeling assumptions, we develop closed form solutions for the expected reduction in misclassification probabilities, and use these for constructing adaptive sampling designs that run in real-time on board the AUV. The contribution extends related work on expected Bernoulli variance reduction (Chevalier et al., 2013; Fossum et al., 2021), and it presents an approach applicable to spatio-temporal domains. In doing so, we combine elements of spatio-temporal GPs, ESs, and AUV technology for an environmental application. Results are compared with state of the art design approaches, as well as with simplified statistical models. Field experiments demonstrate applicability of the methods for real-world environmental sensing.

The article is organized as follows: In Section 2, the SPDE model for concentration is presented. In Section 3, data assimilation is discussed. In Section 4, expected misclassification probabilities associated with the ESs are presented, followed by closed form results for this design criterion and algorithms for autonomous sampling. In Section 5, a simulation study is presented, while real-world experimentation results are in Section 6.

2 | SPATIO-TEMPORAL MODELING OF MINE TAILINGS CONCENTRATIONS

We let $X(t, \mathbf{s})$ denote the pollution concentration at time $t \geq 0$ and spatial (east, north) location \mathbf{s} in a domain $\mathcal{D} \subset \mathbb{R}^2$, $i = 1, \dots, N$. Further, $\mathcal{N}_N(\boldsymbol{\mu}, \boldsymbol{\Sigma})$ denotes a N -variate Gaussian distribution with mean vector $\boldsymbol{\mu}$ and positive definite covariance matrix $\boldsymbol{\Sigma}$.

We model $X(t, \mathbf{s})$ by a SPDE which is outlined in Section 2.1. In the real world, the concentrations are of course not distributed according to this SPDE, and they would most likely be better represented by a full-fledged numerical ocean model simulation. However, the relatively low computer costs of matrix and vector calculations associated with the Gaussian linear SPDE model enable onboard planning of AUV sampling designs, and updating with in-situ concentration data acquired by the AUV. One could say that this SPDE model works as an emulator or surrogate model (Gramacy, 2020) for the complex ocean model. We show how to specify the model parameters of the SPDE from ocean model data in Section 2.2. The updating of the model is in our case based on in-situ measurements. Related statistical emulators for AUV operations with in-situ data in spatial domains have been done in Berget et al. (2018).

2.1 | Advection-diffusion SPDE model

To represent the mine tailings variation in space and time, we use an advection and diffusion model (Sigrist et al., 2015b). This model is linear and Markovian in time. The governing form of the SPDE is

$$\frac{\partial}{\partial t}X(t, \mathbf{s}) = -\mathbf{v}(\mathbf{s})^T \nabla X(t, \mathbf{s}) + \nabla \cdot \mathbf{D} \nabla X(t, \mathbf{s}) + \zeta X(t, \mathbf{s}) + \tilde{R}(t, \mathbf{s}) + \tilde{\eta}(t, \mathbf{s}), \quad (1)$$

where $\mathbf{v}(\mathbf{s}) = (v_e(\mathbf{s}), v_n(\mathbf{s}))^T$ is the drift vector field for the advection (which could in principle depend on time as well), $\mathbf{D} = D\mathbf{I}_2$ the diffusion matrix which is assumed to be isotropic in this work, and $\zeta \in [-1, 0]$ a damping constant controlling the relationship between state vectors in time (see, e.g., Richardson, 2017, Section 3.1). Moreover, $\tilde{\eta}(t, \mathbf{s})$ is an additive SPDE noise term which is assumed to be spatially colored while it is independent over the temporal domain (Sigrist et al., 2015b). The system forcing, such as a point source for the mine tailings or other external information along the boundary, enters via the $\tilde{R}(t, \mathbf{s})$ term.

The SPDE in (1) can be solved in different ways. Sigrist et al. (2015b) use a spectral representation with Fourier terms, and this solution is also implemented as an R package (Sigrist et al., 2015a). Solutions are fast and accurate, but stationarity in space is required, and this is not a plausible assumption in our application. Instead, we use a method of finite differences which is also useful for our purpose of data assimilation and adaptive spatio-temporal sampling. In the discretization of the continuous SPDE, the spatial grid has resolution ds_e in the east direction and ds_n in the north direction. The time is discretized with steps of dt . Forward differences are used in time and central differences in space, giving

$$\begin{aligned} X(t + dt, \mathbf{s}) = & X(t, \mathbf{s}) + dt\tilde{R}(t, \mathbf{s}) + dt\tilde{\eta}(t, \mathbf{s}) + dt \left(\zeta - \frac{2D}{ds_e^2} - \frac{2D}{ds_n^2} \right) X(t, \mathbf{s}) \\ & + dt \left(\frac{v_e}{2ds_e} + \frac{D}{ds_e^2} \right) X(t, \mathbf{s}_E^-) + dt \left(-\frac{v_e}{2ds_e} + \frac{D}{ds_e^2} \right) X(t, \mathbf{s}_E^+) \\ & + dt \left(\frac{v_n}{2ds_n} + \frac{D}{ds_n^2} \right) X(t, \mathbf{s}_N^-) + dt \left(-\frac{v_n}{2ds_n} + \frac{D}{ds_n^2} \right) X(t, \mathbf{s}_N^+), \end{aligned} \quad (2)$$

where $\mathbf{s}_E^\pm = \mathbf{s} \pm (ds_e, 0)^T$ and $\mathbf{s}_N^\pm = \mathbf{s} \pm (0, ds_n)^T$. Alternative schemes are of course possible (Richardson, 2017).

We denote the rectangular discretized spatial grid by $\mathcal{D}_s = \{\mathbf{s}_1, \dots, \mathbf{s}_N\}$, where N is the number of grid cells. With the regular time discretization, we simply denote times by $t = 0, 1, \dots, n$, so $t + 1$ is used instead of $t + dt$. The terms arising from (2) can be collected for all N grid positions to obtain a model representation on vector-matrix form:

$$\mathbf{X}_{t+1} = \mathbf{A}_t \mathbf{X}_t + \mathbf{R}_t + \boldsymbol{\eta}_{t+1}, \quad t = 0, 1, \dots, n-1. \quad (3)$$

Here, $\mathbf{X}_t = (X(t, \mathbf{s}_1), \dots, X(t, \mathbf{s}_N))^T$ is the length N state vector at time step t and \mathbf{A}_t is the $N \times N$ propagator matrix for advection, diffusion and damping from the finite differences in (2). In general, this matrix can vary with time, but for our AUV deployment in a limited time period this matrix is kept fixed so that $\mathbf{A}_t = \mathbf{A}$. The length N vector $\mathbf{R}_t = \mathbf{R}$ is a discretized version of the forcing terms which are also assumed to be temporally constant during the time interval. We further assume constant noise covariance over time; $\boldsymbol{\eta}_{t+1} \sim N_N(\mathbf{0}, \mathbf{Q}_{t+1})$, $\mathbf{Q}_{t+1} = \mathbf{Q}$, and $\boldsymbol{\eta}_{t+1}$ is independent of the variables $\mathbf{X}_0, \dots, \mathbf{X}_t$.

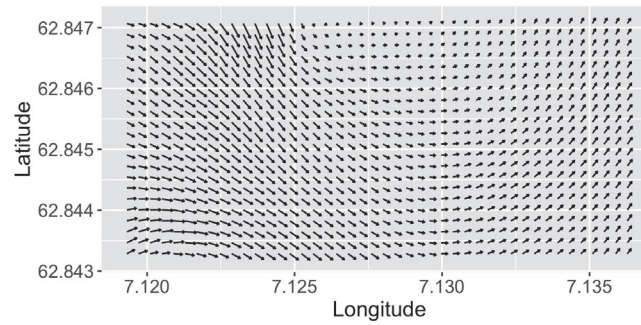


FIGURE 2 Ocean model data from SINMOD. Arrows indicate the advection field in the fjord

We use GP initial conditions, and on the discretized domain we have

$$\mathbf{X}_0 = (X_0(\mathbf{s}_1), X_0(\mathbf{s}_2), \dots, X_0(\mathbf{s}_N))^T, \quad \mathbf{X}_0 \sim \mathcal{N}_N(\boldsymbol{\mu}_0, \boldsymbol{\Sigma}_0). \quad (4)$$

Along with the linear relations in (3), we then have $\mathbf{X}_t \sim N_N(\boldsymbol{\mu}_t, \boldsymbol{\Sigma}_t)$, with recursions

$$E[\mathbf{X}_{t+1}] = \boldsymbol{\mu}_{t+1} = \mathbf{A}\boldsymbol{\mu}_t + \mathbf{R}, \quad \text{Cov}(\mathbf{X}_{t+1}) = \boldsymbol{\Sigma}_{t+1} = \mathbf{A}\boldsymbol{\Sigma}_t\mathbf{A}^T + \mathbf{Q}. \quad (5)$$

The boundary conditions (BCs) for the SPDE must also be considered, and there are several approaches for setting the BCs. Dirichlet BCs require knowledge of the state values, and can be seen as a constant forcing along a boundary. We use this for the boundary side near the source, where variables are replaced by their known values. Neumann BCs with no drift across the boundary of the domain, are used for the remaining three rectangular boundary sides away from the source. All BC terms are added to the \mathbf{R} vector on the right-hand side of (3).

2.2 | Specifying SPDE parameters for Frønfjorden

As previously mentioned, the SPDE model can be regarded as an emulator or surrogate model for the complex numerical solution of the spatio-temporal mine tailings variation. To specify the model parameters of the SPDE model, we hence use data from two numerical ocean models:

- Ocean model current data provided by SINMOD (Slagstad & McClimans, 2005), which is a versatile system for numerical simulation of ocean variables. In our case, this is used to set the advection field \mathbf{v} in the SPDE model.
- Ocean model mine tailings concentration data provided by DREAM (Dose-Related Risk and Effect Assessment Model), which is used for numerical simulation of the transport, exposure, dose and effects of chemicals in marine environments (Rye et al., 2008). Ocean model current data from SINMOD are used as input to this model. In our case, the DREAM data are used to specify the mean and covariance parameters of the statistical model.

We first discuss the use of SINMOD data. Figure 2 shows the average advection field computed from SINMOD. Such data will of course change depending on the considered locations in the fjord and with the day and time of operation. Figure 2 shows a falling-tide average computed over several days of SINMOD data, for the inner part of the fjord. This full-fledged numerical ocean model is very computer intensive, and we only had 17 days of available data. For the drift field \mathbf{v} , it is reasonable to assume constant drift over a short 0.5–1 h AUV operation interval that we considered here.

We next discuss the use of DREAM data. Figure 3 shows transformed log-concentration of mine tailings from DREAM for the inner part of the fjord for two different days. Near the deposition site (marked by a black circle) the concentration is high. We notice that the concentrations in Figure 3 decrease away from this source, and that it tends to move in an anticlockwise motion in the domain, caused by the bathymetry and drift field in the inner fjord.

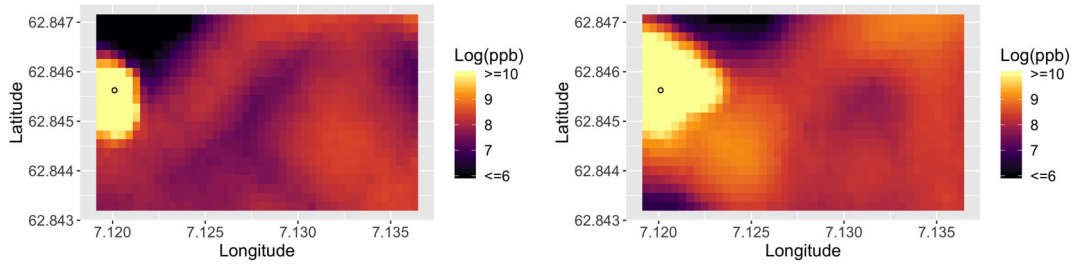


FIGURE 3 Ocean model data from DREAM illustrating falling-tide concentrations at two days (left and right). The source position (circle) has high concentration. The concentration values are visualized on the form $(\log(\text{concentration} + 1))$

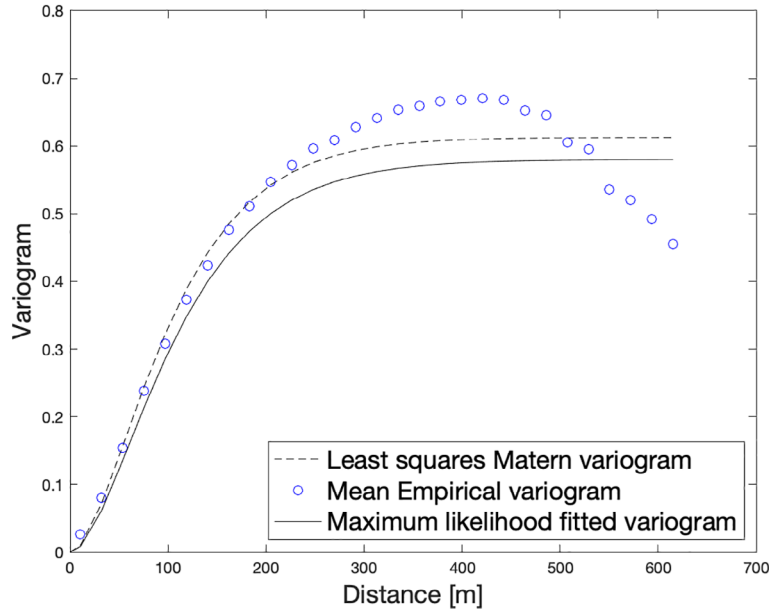


FIGURE 4 Mean empirical variogram together with fitted Matern (3/2 smoothness) variograms using least squares to empirical variograms and maximum likelihood estimation

We use this DREAM data to fit the mean and covariance parameters of the SPDE model. Just like the SINMOD data, we have 17 days of available DREAM data, all at the same falling-tide time intervals. These are treated as realizations of the concentration variable $X(t, \mathbf{s})$. The realizations are considered as independent in our analysis. Within each day, we also have DREAM output samples every minute. This means that we can use the data to set both initial mean and covariance parameters as well as those in the dynamical part.

The initial mean μ_0 in expression (4) is set from the average for each spatial position in the DREAM data at initial time. Notably, this mean hence varies in space. The covariance matrix Σ_0 is specified from the variance and spatial correlation in this initial time data. Figure 4 shows the mean empirical variograms (circles) based on the DREAM realizations. This display also shows the fitted Matern covariance function with smoothness parameter 3/2 using least squares fitting to variograms (dashed) as well as maximum likelihood estimation to the DREAM data (solid). There is only slight difference in these plots, and the spatial variation appears to be represented well with a correlation length of about 500 m and variance of 0.6. In doing this analysis, some of the 17 realizations with very fluctuating or outlying variograms were removed.

The DREAM residuals $\mathbf{X}_{t+1} - (\mathbf{A}\mathbf{X}_t + \mathbf{R})$ are used to specify the covariance matrix \mathbf{Q} . Similar to the initial state analysis, we fit a Matern (3/2) covariance function. The effective correlation range is now estimated to 120 m and the variance parameter is $0.1 \log(\text{ppb})^2$. To help ensure numerical stability and positive definiteness, we add a small nugget effect of 0.01^2 .

There does not seem to be any damping over time in the DREAM data, but for stability reasons (Richardson, 2017) we specify a very small level $\zeta = -0.0010$. As mentioned previously, the damping relates to the concentration reduction over

time, which in our case could describe the decay in mine tailings concentration due to sinking. The diffusion constant D is given as $0.1 \text{ m}^2/\text{s}$, and is hence set to be the same as the diffusion constant used in the DREAM ocean model to create the mine tailings concentration data.

Variations of this model will also be used for comparison in the simulation study: The advection is varied ± 3 standard deviations based on SINMOD variability, away from the benchmark settings. The direction in each position stays the same.

3 | STATE SPACE MODEL AND DATA ASSIMILATION

The concentrations are in our case observed in-situ by deploying an AUV. The mine tailings concentration data that are gathered on board the AUV are used to update the SPDE model. We here outline the state space model, and then use the spatial Kalman filter to assimilate the data recursively over time (Cressie & Wikle, 2011).

We denote the length m vector of measurements at time t by \mathbf{Y}_t , and assume an observation model defined by

$$\mathbf{Y}_t = \mathbf{H}_t \mathbf{X}_t + \boldsymbol{\varepsilon}_t, \quad t = 1, \dots, n, \quad (6)$$

where \mathbf{H}_t is a size $m \times N$ design matrix specifying which grid points are sampled at time step t . Each row of \mathbf{H}_t has a 1 entry on the vector position associated with the observed grid cell and the other entries are 0. The measurement errors have independent and identically distributed elements $\varepsilon_{t,j}$, $j = 1, \dots, m$, which are assumed to be Gaussian distributed with mean zero and standard deviation τ . Moreover, we assume that $\boldsymbol{\varepsilon}_t$ and \mathbf{X}_t are independent. Expression (6) means that $\mathbf{Y}_t | \mathbf{X}_t \sim N_m(\mathbf{H}_t \mathbf{X}_t, \tau^2 \mathbf{I}_m)$. Together with the discretized SPDE model in (3), this defines a state space model for the concentrations and AUV observations.

In the online setting, the goal is to calculate and use the filtering model for concentrations. Denoting the available data at time t by $\mathcal{Y}_{1:t} = (\mathbf{Y}_1, \dots, \mathbf{Y}_t)$, the filtering problem relates to the conditional distribution of \mathbf{X}_t given $\mathcal{Y}_{1:t}$. The predictive distributions of $\mathbf{X}_{t'}$, $t' = t+1, \dots, n$, given $\mathcal{Y}_{1:t}$, could also be of interest. In particular the end time n , which can be considered a decision check point, where one might act to mitigate the concentration levels if they are too high.

In our case with the linear SPDE model and Gaussian measurement models, the conditional distributions of interest are Gaussian. The Kalman filter, see, for example, Särkkä (2013), is used to update the required means and covariance matrices recursively over time. We define the one-step predictive mean $\boldsymbol{\mu}_{t|t-1} = E[\mathbf{X}_t | \mathcal{Y}_{1:t-1}]$ and covariance matrix $\boldsymbol{\Sigma}_{t|t-1} = \text{Cov}(\mathbf{X}_t | \mathcal{Y}_{1:t-1})$. Likewise, after data assimilation, we have the updated (filtering) mean $\boldsymbol{\mu}_{t|t} = E[\mathbf{X}_t | \mathcal{Y}_{1:t}]$ and covariance matrix $\boldsymbol{\Sigma}_{t|t} = \text{Cov}(\mathbf{X}_t | \mathcal{Y}_{1:t})$. The Kalman filter recursions use prediction and updating steps. From expression (3), the prediction step is

$$\boldsymbol{\mu}_{t|t-1} = \mathbf{A} \boldsymbol{\mu}_{t-1|t-1} + \mathbf{R}, \quad \boldsymbol{\Sigma}_{t|t-1} = \mathbf{A} \boldsymbol{\Sigma}_{t-1|t-1} \mathbf{A}^T + \mathbf{Q}. \quad (7)$$

The formulas for the updated mean and covariance matrix at time t are

$$\boldsymbol{\mu}_{t|t} = \boldsymbol{\mu}_{t|t-1} + \mathbf{K}_t (\mathbf{y}_t - \mathbf{H}_t \boldsymbol{\mu}_{t|t-1}), \quad \boldsymbol{\Sigma}_{t|t} = (\mathbf{I}_N - \mathbf{K}_t \mathbf{H}_t) \boldsymbol{\Sigma}_{t|t-1}, \quad (8)$$

where the $N \times m$ matrix $\mathbf{K}_t = \boldsymbol{\Sigma}_{t|t-1} \mathbf{H}_t^T \mathbf{S}_t^{-1}$ is the Kalman gain and the $m \times m$ innovation covariance matrix $\mathbf{S}_t = \mathbf{H}_t \boldsymbol{\Sigma}_{t|t-1} \mathbf{H}_t^T + \tau^2 \mathbf{I}_m$.

To find the distribution of \mathbf{X}_n , given $\mathcal{Y}_{1:t}$, we take $n - t$ prediction steps, with no updating. The predictive mean and covariance matrix are then

$$\begin{aligned} \boldsymbol{\mu}_{n|t} &= \mathbf{A}^{n-t} \boldsymbol{\mu}_{t|t} + (\mathbf{A}^{n-t-1} + \mathbf{A}^{n-t-2} + \dots + \mathbf{A} + \mathbf{I}) \mathbf{R}, \\ \boldsymbol{\Sigma}_{n|t} &= \mathbf{A} (\dots (\mathbf{A} (\mathbf{A} \boldsymbol{\Sigma}_{t|t} \mathbf{A}^T + \mathbf{Q}) \mathbf{A}^T + \mathbf{Q}) \dots) \mathbf{A}^T + \mathbf{Q}. \end{aligned} \quad (9)$$

4 | AUTONOMOUS SAMPLING DESIGNS

We develop sampling design strategies for mapping the spatio-temporal concentration variable. For this task, a criterion is needed to evaluate the possible sampling designs. The aim is often to reduce expected uncertainty in some sense (Azzimonti et al., 2016; Bect et al., 2012; Eidsvik et al., 2015). The focus of this article is on reducing the expected

probabilities of misclassifications in the ES. These are computed at a target time ahead in the sampling interval and averaged over the entire spatial domain.

After introducing ESs, associated excursion probabilities (EPs) and the misclassification criterion, we derive a closed-form solution for this criterion under the Gauss-linear modeling assumptions. We then put it all in the context of adaptive AUV sampling.

4.1 | Excursion sets

ESs indicate where the variables of interest are above some critical limit. Identifying ESs is important in several environmental applications (Angulo & Madrid, 2010; French & Sain, 2013). Let l be the critical limit of the system. A random ES over the domain \mathcal{D}_s at time t' is here defined as

$$\text{ES}_{t'} = \{\mathbf{s}_i \in \mathcal{D}_s : X_{t'}(\mathbf{s}_i) > l\}. \quad (10)$$

In this context, t' is a particular time of interest, where one in our case can possibly take some action to mitigate the concentration level by for instance reducing the mining deposition rates. This reference time will typically be the latest monitoring time $t' = n$. Note that expression (10) defines just one of several kinds of ESs (Bolin & Lindgren, 2015, 2018).

Just before time $t \leq t'$, assume data $\mathcal{Y}_{1:t-1}$ is available. The marginal EPs associated with the ES in (10) are

$$\text{EP}_{t'}(\mathbf{s}_i) = P(X_{t'}(\mathbf{s}_i) > l | \mathcal{Y}_{1:t-1}), \quad \mathbf{s}_i \in \mathcal{D}_s. \quad (11)$$

From these EPs, the mean misclassification probability (MMP) is defined by

$$\text{MMP}_{t'} = \frac{1}{N} \sum_{i=1}^N \min\{1 - P(X_{t'}(\mathbf{s}_i) > l | \mathcal{Y}_{1:t-1}), P(X_{t'}(\mathbf{s}_i) > l | \mathcal{Y}_{1:t-1})\}. \quad (12)$$

This MMP is dominated by the probabilities that are near 0.5.

At time t , the design question relates to the augmentation of data $\mathcal{Y}_{1:t-1}$ with a random sample \mathbf{Y}_t^d according to design d which is highlighted in the notation. This design must be among the possible designs $\mathcal{D}_t \subset \mathcal{D}_s$ at that time. There are several strategies for selecting the design. For the optimal design choice at time t , one must in principle consider all possible positions and measurement values for steps $t + 1, \dots, n$. This becomes an intractable optimization problem involving a sequence of interrelated minimizations and integrals. Instead, we present heuristic methods considering only the current time step.

While we discuss various heuristics that can be run onboard the AUV in Section 4.3, we focus here on a myopic strategy that is statistically optimal according to the expected MMP (EMMP) when assuming that one conducts no more measurements after time t . The optimal design is then

$$\begin{aligned} d_t^* &= \operatorname{argmin}_{d \in \mathcal{D}_t} \text{EMMP}_{t'}^d, \\ \text{EMMP}_{t'}^d &= \int_{\mathbf{Y}_t^d} \frac{1}{N} \sum_{i=1}^N \min\{1 - p_{i,t'}^d, p_{i,t'}^d\} p(\mathbf{y}_t^d | \mathcal{Y}_{1:t-1}) d\mathbf{y}_t^d, \\ p_{i,t'}^d &= P(X_{t'}(\mathbf{s}_i) > l | \mathcal{Y}_{1:t-1}, \mathbf{Y}_t^d), \end{aligned} \quad (13)$$

where $p(\mathbf{y}_t^d | \mathcal{Y}_{1:t-1})$ is the probability density function (pdf) of \mathbf{Y}_t^d , conditioned on the previous samples $\mathcal{Y}_{1:t-1}$.

In the spatio-temporal sampling scheme, the choice of design is done conditional on all data up to time $t - 1$, and the probabilities can be computed for a future time t' , while the expectation is over data at time t . The choice d determines the 1 and 0 structure of the design matrix $\mathbf{H}_t = \mathbf{H}_t^d$ in (6), where the design is again highlighted in the superscript. Of course, the available data $\mathcal{Y}_{1:t-1}$ were also gathered according to a chosen design, but this is ignored in the notation. The only effect of this design is via the conditioning in the probabilistic model and the current position which determines the design set \mathcal{D}_t .

4.2 | Closed form expressions for EMMP

From the data assimilation expressions (7) and (8), we have the predictive Gaussian distribution for $X_{t'}(\mathbf{s}_i)$. Moreover, just before time t , the predictive distribution for the next observation is $\mathbf{Y}_t^d | \mathcal{Y}_{1:t-1} \sim N(\mathbf{H}_t^d \boldsymbol{\mu}_{t|t-1}^d, \mathbf{S}_t^d)$. The superscript d notation is included again to emphasize the dependence on the design.

To facilitate the EMMP calculations in (13), we introduce variables

$$U_i^d = \frac{l - \mu_{t'|t}^d(i)}{\sqrt{\Sigma_{t'|t}^d(i, i)}}, \quad i = 1, \dots, N. \quad (14)$$

Here, $\mu_{t'|t}^d(i)$ is the i th component of the predictive mean and $\Sigma_{t'|t}^d(i, i)$ the i th diagonal element of the predictive covariance matrix (see expression (9)), after the assimilation of $\mathcal{Y}_{1:t-1}$ and the new sample \mathbf{Y}_t^d . The random variable U_i^d is linearly related to \mathbf{Y}_t^d via $\mu_{t'|t}^d(i)$, and it is hence Gaussian distributed. One can regard this as a transformed variable of the unknown data outcome at time t for the given design d . Because of its direct link to the probabilities in (13), the expression for EMMP is equivalent to N univariate integrals (Bhattacharjya et al., 2013; Chevalier et al., 2013), one for each of $U_i^d, i = 1, \dots, N$.

In mathematical terms, the relations in (8) mean that we have

$$\begin{aligned} E[U_i^d | \mathcal{Y}_{1:t-1}] &= \mu_{u_i^d} = \frac{l - E[\mu_{t'|t}^d(i) | \mathcal{Y}_{1:t-1}]}{\sqrt{\Sigma_{t'|t}^d(i, i)}} = \frac{l - \mu_{t'|t-1}^d(i)}{\sqrt{\Sigma_{t'|t}^d(i, i)}}, \\ \text{Var}(U_i^d | \mathcal{Y}_{1:t-1}) &= \sigma_{u_i^d}^2 = \frac{1}{\Sigma_{t'|t}^d(i, i)} \text{Var}(\mu_{t'|t}^d(i) | \mathcal{Y}_{1:t-1}) \\ &= \frac{1}{\Sigma_{t'|t}^d(i, i)} \mathbf{A}^{t'-t}(i, i) \mathbf{K}_t^d \mathbf{S}_t^d (\mathbf{A}^{t'-t}(i, i) \mathbf{K}_t^d)^T, \end{aligned} \quad (15)$$

where $(i,)$ indicates row i of the matrix. We let $p(u_i^d)$ denote the Gaussian pdf with mean and variance defined in (15). The EMMP in (13) is then given by

$$\text{EMMP}_{t'}^d = \frac{1}{N} \sum_{i=1}^N \int_{u_i^d} \min \{ \Phi(u_i^d), 1 - \Phi(u_i^d) \} p(u_i^d) du_i^d = \frac{1}{N} \sum_{i=1}^N \text{EMP}_{i,t'}^d, \quad (16)$$

where $\text{EMP}_{i,t'}^d$ is the expected misclassification probability in position \mathbf{s}_i . Moreover, $\Phi(u_i^d) = P(Z \leq u_i^d) = \int_{-\infty}^{u_i^d} p(z) dz$ represents the cumulative distribution function (cdf) of a standard normal variable Z . By symmetry $1 - \Phi(u_i) = \Phi(-u_i)$, and since Φ is monotonically increasing, the integral over u_i can be split in two parts;

$$\text{EMP}_i^d = \int_{-\infty}^0 \Phi(u_i^d) p(u_i^d) du_i^d + \int_0^{\infty} \Phi(-u_i^d) p(u_i^d) du_i^d. \quad (17)$$

Defining Z and U_i^d to be independent, so that $p(z)p(u_i^d)$ is their joint density function, we get

$$\int_{-\infty}^0 \Phi(u_i^d) p(u_i^d) du_i^d = \int_{-\infty}^0 \int_{-\infty}^{u_i^d} p(z) p(u_i^d) dz du_i^d = P(Z < U_i^d, U_i^d < 0). \quad (18)$$

By the same argument for the second integral in (17), we have

$$\begin{aligned} \text{EMP}_i^d &= P(Z < U_i^d, U_i^d < 0) + P(Z < -U_i^d, U_i^d > 0) \\ &= P(Z - U_i^d < 0, U_i^d < 0) + P(Z + U_i^d < 0, -U_i^d < 0). \end{aligned} \quad (19)$$

The bivariate distributions of Z and U_i^d are used next. For the first term

$$\begin{bmatrix} Z - U_i^d \\ U_i^d \end{bmatrix} = N_2(\boldsymbol{\mu}_i^{\dagger d}, \boldsymbol{\Sigma}_i^{\dagger d}), \quad \boldsymbol{\mu}_i^{\dagger d} = \begin{bmatrix} -\mu_{u_i^d}^d \\ \mu_{u_i^d}^d \end{bmatrix}, \quad \boldsymbol{\Sigma}_i^{\dagger d} = \begin{bmatrix} \sigma_{u_i^d}^2 + 1 & -\sigma_{u_i^d}^2 \\ -\sigma_{u_i^d}^2 & \sigma_{u_i^d}^2 \end{bmatrix}, \quad (20)$$

and a similar expression holds for the second term in (19). We then get

$$\text{EMP}_i^d = \Phi_2(\mu_i^{\dagger d}, \Sigma_i^{\dagger d}) + \Phi_2(-\mu_i^{\dagger d}, \Sigma_i^{\dagger d}), \quad (21)$$

where Φ_2 is the bivariate cdf evaluated at $\mathbf{0} = (0, 0)^T$.

4.3 | Adaptive sampling with an AUV

Expression (13) is the foundation for the suggested AUV sampling design scheme. At every step t , (i) the model is updated using an observation from the current AUV location, (ii) the next optimal sampling design d_t^* is selected based on the smallest EMMP. The possible designs D_t are here defined via a waypoint graph (grid), where each possible new waypoint is located between a minimum and maximum travel distance from the AUV position at time t . By keeping the allowable travel range relatively small, the cost of traveling to a new location is approximately the same for each step, in our case about 25 m. Even though the AUV has limited computational resources, the closed form solution of EMMP provided by (16) and (21) enable efficient calculation of the possible designs in a few seconds, and this allows near real-time AUV operation.

The myopic approach is suboptimal because it only looks at the current stage t . To avoid getting stuck in a local minima, we test a hybrid strategy, where we combine the suggested myopic approach with another criteria that minimizes the integrated reduction in variances; $\text{trace}(\Sigma_{t|t-1} - \Sigma_{t|t}^d)$. In doing so, the AUV can move away from regions that have been sampled rather accurately, to regions that have larger variability. This hybrid strategy is trying to balance exploration of the domain and exploitation of known information. We use a ϵ -greedy approach (Zhang & Angela, 2013), where the AUV is programmed to select the next design for variance exploration with probability $1 - \epsilon$, and otherwise finds the next design based on (local waypoint) EMMP. There are many different approaches for tuning ϵ and conducting these kinds of hybrid strategies. We use the same criterion for k consecutive steps. In the beginning, ϵ is quite high, as we want the default to be the EMMP criterion. The number of times the AUV has been inside a circle of radius r from the current position is then calculated, and the probability ϵ is reduced by a factor proportional to this recurrence fraction.

We compare results of the suggested strategies with several other simpler strategies (listed and described in Table 1). A useful reference is the naive strategy which chooses design positions randomly among the possible neighborhood grid cells at every time step. We also study the strategy choosing the design based on the waypoint grid node with EP_t (expression 11) closest to 0.5. In addition, we compare results with two pre-scripted designs, which do not have any kind of adaptation. One of these is designed to move diagonally in western parts known to be interesting based on visual inspection of concentration data. The other pre-scripted design is a more traditional one starting at the southern central line and moving north in a lawn-mower pattern.

TABLE 1 Description of the different sampling design strategies

Case	Description
SPDE: EMMP _n	Minimizing EMMP within local waypoint graph designs and at future time n .
SPDE: EMMP _t	Minimizing EMMP within local waypoint graph designs and at current time t .
SPDE: Hybrid	Blend of random transects and SPDE: EMMP _t at time t .
SPDE: Random	Choose randomly within local waypoint graph designs at each time t .
SPDE: EP _t 0.5	Choose local waypoint graph designs with EP closest to 0.5 at current time t .
SPDE: Pre-diag	Sample selected pre-scripted diagonal transects design, with no adaptation.
SPDE: Pre-lawn	Sample along a lawn-mower pre-scripted design, with no adaptation.
AR(1): EMMP _n	Same as SPDE: EMMP _n , but with a spatial AR(1) model.
Spatial: EMMP	Same as SPDE: EMMP _t , but with only spatial variability and no time dynamics.

Note: Bottom two rows differ in terms of modeling.

We further compare results of using simpler statistical models for the space-time variability. One alternative model is a spatial autoregressive (AR) model (see, e.g., Cressie & Wikle, 2011, Section 6.4). In our case, we specify an AR(1) model using the same autoregressive parameter for all spatial locations. This parameter is estimated from the sample correlation in the available oceanographic DREAM data. The other alternative model is a purely spatial model, without time dynamic development. In the comparison with simpler models, the replicate data are still simulated from the specified SPDE model.

5 | SIMULATION STUDY

5.1 | Case description

In this simulation study, we mimic a situation with large discharge from location marked 1.2 in Figure 1. The outlets of mine tailings happen at depth 20 m. A two-dimensional regular rectangular spatial grid is formed at this depth for the inner part of the fjord. The domain has $N_e = 44$ grid nodes in the east-west direction and $N_n = 22$ nodes in the north-south direction, so $N = 968$. There are approximately 20 m between each grid node in both directions. In simulations, we use 1-min time steps in a 30-min interval of interest, just before low tide.

To gain insight in the statistical properties of methods, we use 1000 replicate realizations of the fitted SPDE model (Section 2.2), and go through with the presented sampling strategies (Table 1) for each replicate run. We set the measurement error standard deviation to $\tau = 0.316 \log(\text{ppb})$. At every time step, $m = 1$ data sample is followed by model updating. The ES at time step $n = 30$ is of main interest. The critical concentration limit is set to $l = 8.5 \log(\text{ppb})$, but note that this limit will vary from the operational objective.

5.2 | Performance measures

The main design criterion is the EMMP, and it is natural to compare results based on the realized MMP. After each replicate run with its sampling path and data $\mathcal{Y}_{1:n}$, we hence compute $\frac{1}{N} \sum_{i=1}^N \min\{1 - P(X_n(\mathbf{s}_i) > l | \mathcal{Y}_{1:n}), P(X_n(\mathbf{s}_i) > l | \mathcal{Y}_{1:n})\}$. Further, actual misclassification rates for the predictions can be calculated based on the final predictions and the true ES at time n . A probability cutoff of 0.5 is used for EP_n , and the average misclassification rate for a replicate run is then $\frac{1}{N} \sum_{i=1}^N I(I(\text{EP}_n(\mathbf{s}_i) \geq 0.5) \neq \text{ES}_n(\mathbf{s}_i))$, where $\text{ES}_n(\mathbf{s}_i)$ is the actual indicator variable of the ES for location \mathbf{s}_i at time n .

We also compare how well the concentration prediction at time step n matches the actual concentration at that time. This is done via the mean squared error (MSE), averaged over all sites and for the 1000 replicates.

The various strategies demand different amounts of calculations. In a real-world operation, the AUV stops to do calculations for a short while at a waypoint, but this time should not be significant compared with the time used between waypoints. We study the approximate computation times for obtaining one sampling path with each strategy using a MacBook Pro 2015 laptop with i5 core. This is not an unrealistic comparison with the computing resources on board the AUV, where the embedded system is operating on a NVIDIA Jetson TX1 single board computer.

5.3 | Results

We first compare the strategies based on using only the next time step ($t' = t$) and that of always predicting to the end point ($t' = n$). We denote results of these two by $\{\text{SPDE: EMMP}_t\}$ and $\{\text{SPDE: EMMP}_n\}$, respectively. The second approach which is using the SPDE model all the way to n is more realistic, but the approach is still only myopic in the strategic selection, and there might not be significant gains in the results.

Figure 5 displays example sampling paths made by these two different adaptive strategies (n middle, t bottom) for two replicates (left, right). The paths are sketched on the final step EPs, which are conditional on all the sampled data in that run. The true ES_n is also shown (top). In the leftmost replicate, neither $\{\text{SPDE: EMMP}_n\}$ nor $\{\text{SPDE: EMMP}_t\}$ strategies are able to map all parts of the ES, but they both map the western part well. In the rightmost display, they cover a larger part of the domain and predict the true ES more accurately. Figure 5(d) shows that the end strategy maps the northern part well, but misses the south-eastern part. It is the other way around for the strategy only predicting one step (Figure 5(f)).

Results of course vary over replicates. Table 2 shows that the misclassification and MSE measures are about the same for the two methods when we average over the 1000 replicates. The slight improvement of using $\{\text{SPDE: EMMP}_n\}$ seems

Example paths

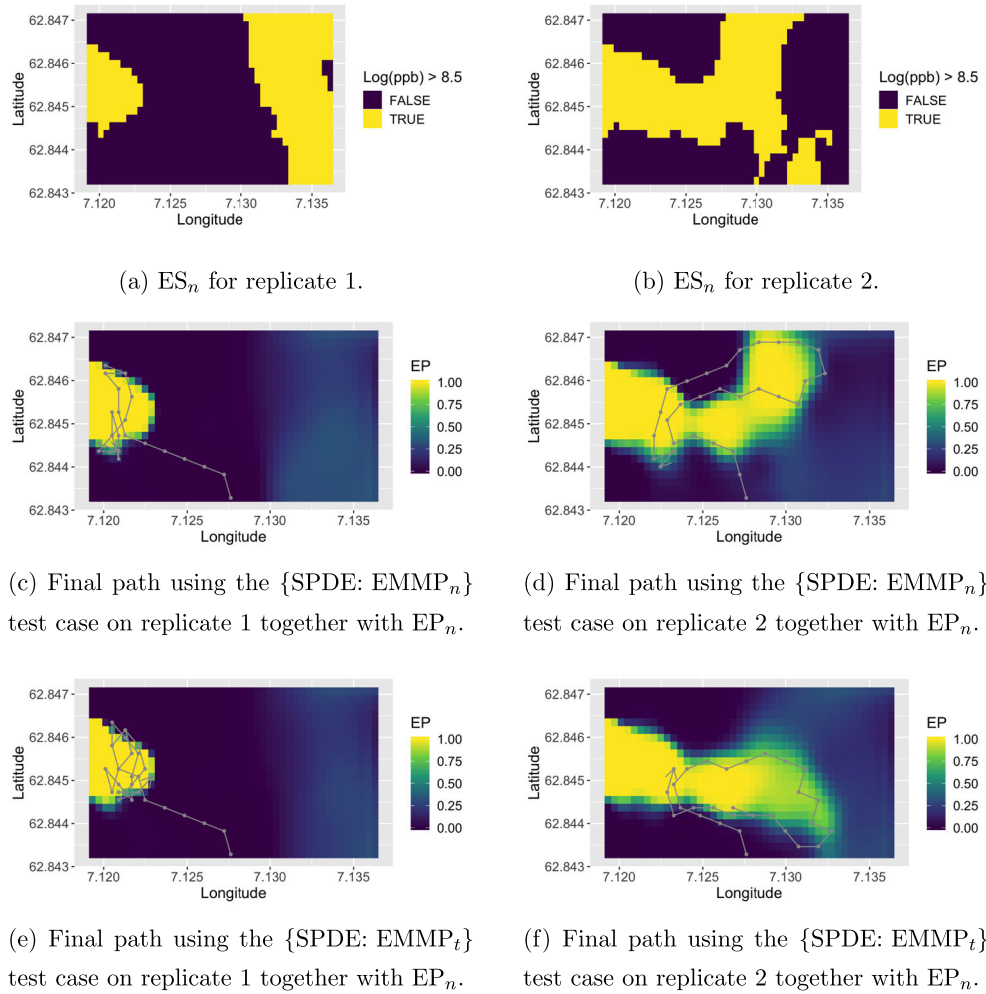


FIGURE 5 Final simulated AUV paths for two replicates and the two test cases $\{SPDE: EMMP_n\}$ and $\{SPDE: EMMP_t\}$. The paths are displayed together with the final EPs. The true ES at time step n is in the top row

TABLE 2 Comparison of different sampling design strategies

Test case	Mean MMP	Mean misclass. rate	Mean MSE	Comp time (s)
SPDE: $EMMP_n$	0.104	0.103	0.273	40
SPDE: $EMMP_t$	0.103	0.105	0.276	3
SPDE: Hybrid	0.097	0.099	0.224	4
SPDE: Random	0.131	0.131	0.316	0.1
SPDE: EP_t 0.5	0.115	0.119	0.331	2
SPDE: Pre-diag	0.095	0.097	0.165	–
SPDE: Pre-lawn	0.118	0.119	0.232	–
AR(1): $EMMP_n$	0.132	0.135	0.482	8
Spatial: EMMP	0.112	0.140	0.486	1.5

Note: Bottom row shows results of the AR(1) and spatial model, all others use the SPDE model.

Example paths

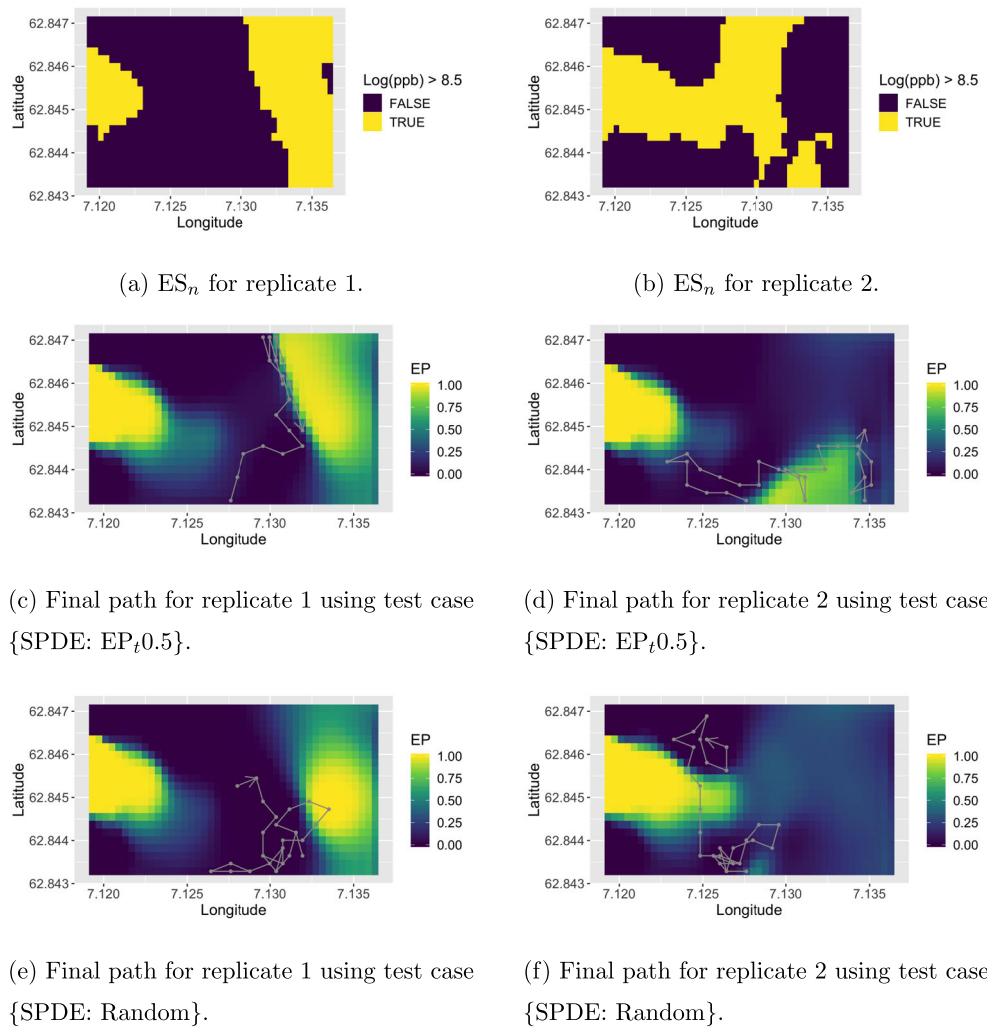


FIGURE 6 Final simulated paths for two sampled replicates and the two test cases $\{SPDE: EP_t 0.5\}$ and $\{SPDE: Random\}$. The paths are displayed together with the final EPs. The true ES at time step n is in the top row

insignificant, especially so considering the ten-fold increase in computer time when doing the forward prediction in (9). It hence seems reasonable to use just time t in this kind of adaptive strategies.

As indicated in Figure 5, the strategies are sometimes missing parts of the ES when the ES is divided into two or more separate regions. The one step ahead strategies prioritize designs with high immediate reward, in the form of reduced EMMP. With the hybrid strategy the AUV can more easily move across such low-reward domains. Table 2 shows that this strategy has somewhat reduced misclassification rates, at the cost of slightly larger computing time. Because the hybrid strategy tends to explore more of the domain, the MSE gets smaller.

We next compare results with that of simpler strategies choosing the next design at random or via the local waypoint with EP closest to 0.5. Paths for the same replicates are shown in Figure 6. The AUV movements are clearly different, but the $\{SPDE: EP_t 0.5\}$ strategy tries to explore the domain in a similar fashion to the myopic EMMP strategy, without really succeeding to the same extent because there is no expected reduction involved in its computations. Replicate results summarized in Table 2 show that the MMPs and MSE are clearly larger for both these strategies.

Now consider the two designs using pre-scripted plans (Figure 7). Table 2 shows that the lawn-mower design $\{SPDE: Pre-lawn\}$ gives larger misclassification rates than strategies $\{SPDE: EMMP_n\}$ and $\{SPDE: EMMP_t\}$, while using the diagonal design $\{SPDE: Pre-diag\}$ gives lower misclassification rates, on par or even better than the adaptive strategies. Guided by preliminary runs, this path is chosen to explore as much of the interesting domain as possible within the time restrictions. Since the ES is often divided into separate parts, which are rarely discovered using the myopic EMMP strategy, the

Example paths

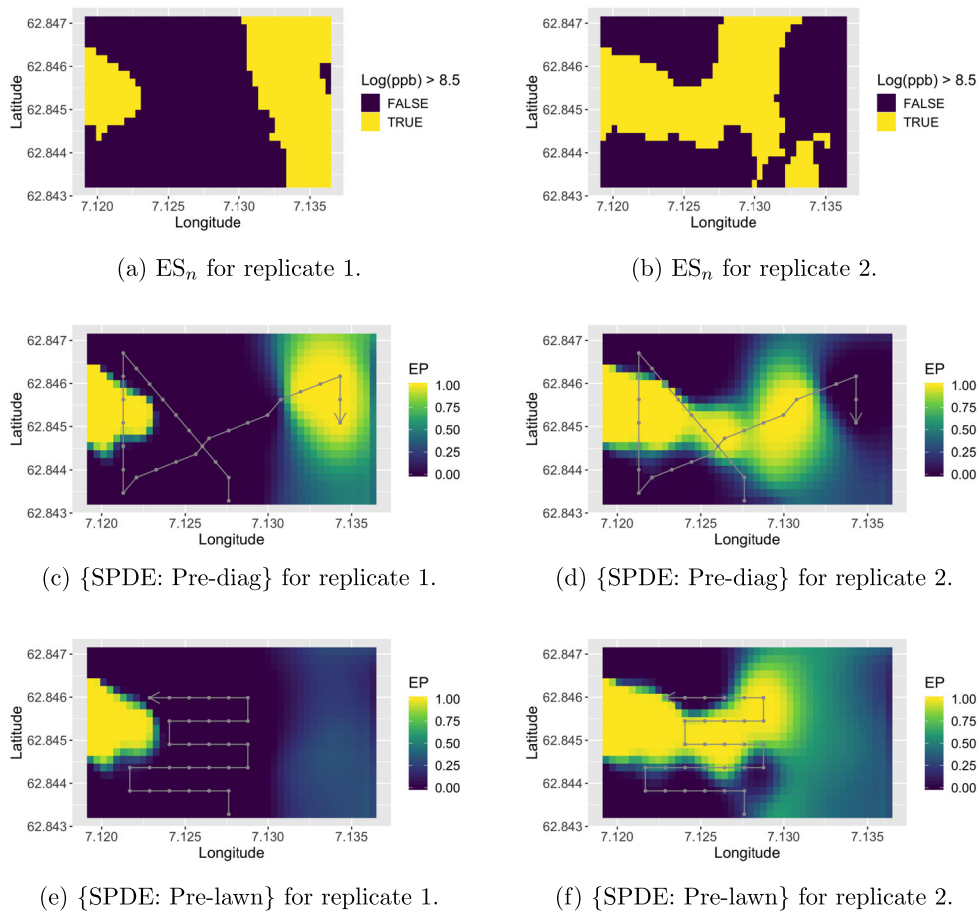


FIGURE 7 Final simulated paths of {SPDE: Pre-diagonals} and {SPDE: Pre-lawn} for two replicates. The paths are displayed together with the final EPs. The true ES at time step n is in the top row

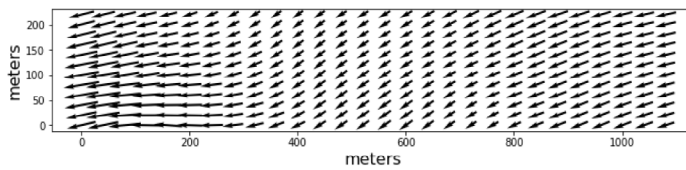
{SPDE: Pre-diag} design has an advantage. The big areas are usually discovered, though some details might be missing, and hence the MSE is small both for {SPDE: Pre-diag} and {SPDE: Pre-lawn}. The EMMP criterion is developed to reduce the probability of misclassification with respect to ESs, and prediction of concentration at positions where it is certain to be above or below the critical limit of the ES does not help classification. Thus, it is expected that strategies with paths covering more of the domain result in smaller MSEs.

Table 2 further shows results of using the EMMP strategies on mis-specified models (AR(1) and spatial model with no temporal dynamical model). The misclassification rates are clearly larger here, and so are the MSEs, meaning that the strategies now get stuck in regions in space and time that are not really of main interest.

We further tested the strategies under different inputs, in particular the advection strength. When drift speed is low, both {SPDE: Pre-diag} and {SPDE: Hybrid} have a misclassification rate of 10.7%. For high advection, the {SPDE: Hybrid} strategy has average misclassification rate of 9.4%, which is lower than the 9.6% of the {SPDE: Pre-diag}. Recall that this pre-scripted path is designed to move across the areas with much prior uncertainty with respect to the reference model. When the advection field is changed, these positions no longer capture the same degree of information. More sensitivity studies are conducted in Foss (2019).

6 | FIELD EXPERIMENTS IN FRÆNFJORDEN

To verify the method's ability to detect an ES containing high concentration of mine tailings particles, a real-life experiment was conducted in Frænfjorden. The experiment was carried out on September 17, 2020. The operational discharge



(a) The drift field v used in the field experiments.



(b) The Light AUV Harald from OceanScan used in the field experiments.

FIGURE 8 The drift field used in the field experiments and the AUV

at the time of the experiments is marked as 2.4 in Figure 1, and an operational area on the west side of the outlet of size $1140 \text{ m} \times 240 \text{ m}$ was used. The predicted drift field at 20 m depth at the time of the experiment is shown in Figure 8(a) (from SINMOD). As seen in the display, the currents were mainly flowing outward of the fjord (toward south-west) at the time.

6.1 | Experimental setup

The robotic platform (see Figure 8(b)) consisted of a Light AUV from OceanScan equipped with a Wetlabs EcoPuck sensor measuring among others total suspended matter (TSM) which was used as the sensor reading for updating the model. Our code was implemented as a python plug-in, running as a part of the autonomous agent architecture Teleo-Reactive Executive (T-REX) (see, e.g., Rajan & Py, 2012). T-REX enables an adaptive mission by communicating with the Unified Navigation Environment (DUNE) which can be seen as the operating system on the AUV, handling control, navigation, communication, vehicle supervision and interaction with actuators and sensors.

The size 57×12 regular two-dimensional grid inside the operational area means that $N = 684$. The distance between each node was approximately 20 m in both grid directions. In order to reduce risk and avoid too much vehicle drift, the AUV was set to move in a yo-yo motion between the surface and the target near 20 m depth. By doing so, the distance between each new chosen neighboring waypoint was between 270 and 290 m, and considering the AUV speed (about 1.2 m/s), the travel time between each waypoint was around 4 minutes.

The measurement error variance τ^2 is not easily set as there are several factors involved (Cetinić et al., 2009; Rogowski et al., 2013). In particular, the measured quantity is optical backscattering in form of an attenuation coefficient indicating turbidity, which is converted to a measure of (log) concentration. There is some uncertainty in this transformation. The Wet Labs ECO 3 sensor user manual suggests an attenuation error of about 4% at attenuation coefficient 1 m^{-1} . Since the log concentrations in the area vary between approximately 3 and 8 log(ppb), assuming measurement error standard deviation of 4% of the log concentration values gives τ between 0.12 and 0.32 log(ppb). But other considerations must also be considered here; for instance vehicle drift which leads to uncertainty in the sampling location, and one way to reflect this uncertainty in our model is to increase τ . Hence, for the real-life experiments we set $\tau = 0.5$.

The SPDE parameters in the field experiments were specified as explained in Section 2.2, but now using ocean model data from the western spatial domain, and for the day and operation time of the mission. The fitted Matern 3/2 model now has parameters $\phi = 120 \text{ m}$ and $\sigma^2 = 0.1 \text{ log(ppb)}^2$. Again, Dirichlet BCs were used for the boundary near the source using DREAM-predictions as the values on this boundary side. For the rectangle sides away from the source, Neumann BCs were used.

6.2 | Results

We used the $\{\text{SPDE: EMMP}_t\}$ strategy to choose the next waypoint in the field experiments. This strategy was run for a total of $n = 12$ time steps, and a critical limit $l = 4.5 \text{ log(ppb)}$ was used. Figure 9 summarizes the mine tailings

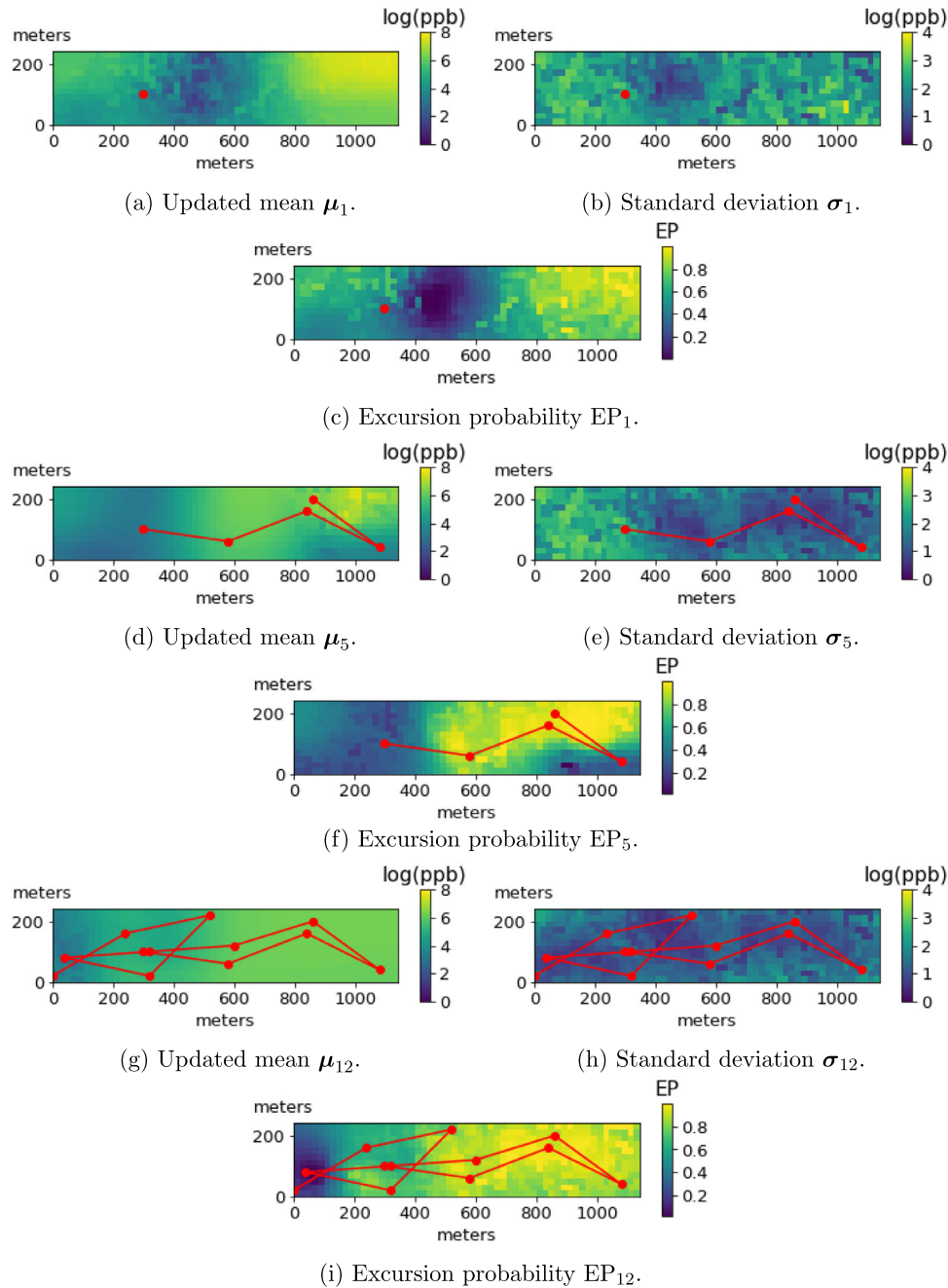


FIGURE 9 Predicted state at selected time steps. The selected waypoints are plotted as a red dot and the red line shows the AUV path up until the given time

concentration distribution at selected time steps of this procedure. The displays indicate updated mean (left), standard deviation (right), and EPs (middle). The resulting AUV path is also plotted as a red line and the waypoints as dots.

Since there exists no ground truth for this case, evaluation of the results is difficult. Still, we are able to see that the method behaves in the way we expect. In the beginning of the mission, the AUV traverses from west to the east side close to the outlet. Then it heads back west and focuses on the area of the predicted boundary of the ES. Comparing the standard deviations at the beginning of the mission with the standard deviations at the end of the mission, we see that the uncertainty in the model is clearly reduced. The results are clearly refined from that of SINMOD and DREAM data alone (top), when AUV data are assimilated in the model (bottom rows). Also, the EPs show that the mine tailings concentrations tend to move further to the left in the lower part of the grid. This appears natural from the physics induced by the advection field in Figure 8(a), but is far from apparent based on the initial model (top).

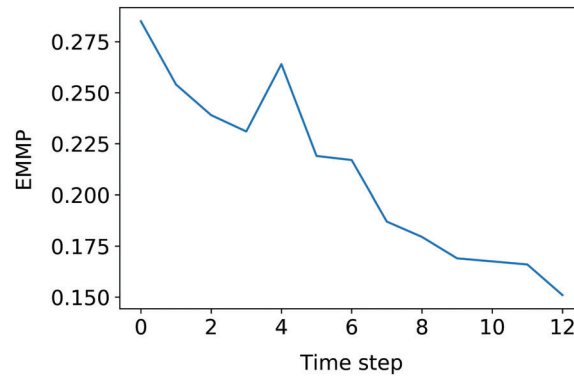


FIGURE 10 $EMMP_t$ computed at each time step t of the operation

Figure 10 shows the $EMMP_t$ over all the grid nodes at each time step. The $EMMP_t$ is clearly decreasing over time, indicating that our method chooses informative waypoints. The exception is at time $t = 4$ where there is a slight increase. By taking a closer look at the data, this occurs because of a surprisingly small concentration ($4.21 \log(\text{ppb})$) in a location quite close to the source (lower, right corner in Figure 9(d)). Since the model expected a higher concentration at this location, and because the in-situ value is quite close to the critical limit $l = 4.5 \log(\text{ppb})$, the update at $t = 4$ led to an increase in the $EMMP$.

7 | CONCLUSIONS

There is currently an enormous development in sensor technologies and robotic autonomous systems that can deploy these new tools in harsh environments such as the oceans. Their use can clearly benefit from realistic statistical modeling and design methods, for instance in the context of where and when to sample an environmental phenomenon as we demonstrate in this work. We fit a spatio-temporal stochastic advection-diffusion model from ocean model data, and use this to represent the mine tailings concentration variables near a mining deposit site in a Norwegian fjord. The AUV has this model on board its computing units, where its path is adapted based on the observations and with the goal of reducing the misclassification probabilities of the ESs of high and low concentration levels.

Simulation results show that a hybrid strategy using a myopic approach combined with a random detour is performing much better than naive strategies. Also, the careful spatio-temporal modeling provides more accurate results than simpler spatial or autoregressive models. In field results, the adaptive sampling procedure gives reasonable results in the sense that the vehicle focuses on the expected boundary regions of high and low concentration, and at the end of operation the EPs are close to 0 or 1. The results further indicate that the ESs obtained from the autonomous surveying can be interpreted from the physical conditions of the ocean currents and the mining deposit site, and more so than from the ocean model data alone.

Further work includes three-dimensional modeling which would extend the current work only looking at 20 m depth. This is of course more demanding from a computational viewpoint, but it would make the data assimilation much more realistic and avoid two-dimensional projection approximations in the AUV waypoint planning. It would also be interesting to include uncertainty in the advection field. A full-fledged stochastic model for this current field would likely not be possible to embed on the onboard computing resources, but a mixture SPDE model over a few scenarios of current fields might work. In the future, we also plan to study the advantages of using two or more autonomous vehicles. This should provide additional spatio-temporal coverage and added flexibility in designs, but such operations also require new elements related to communication and vehicle control.

ACKNOWLEDGMENTS

We acknowledge support from Norwegian Research Council (RCN) through Centers of Excellence funding scheme, Project number 223254—Centre for Autonomous Marine Operations and Systems (NTNU-AMOS), the INDORSE project 267793 and the MASCOT project 305445. The authors would like to thank Frédéric Py from Sintef Digital for helping during the field experiments, and Tor Nordam and Finn Are Michelsen from SINTEF

Ocean for running the numerical models SINMOD and DREAM, and supplying the data sets used in this article.

CONFLICT OF INTEREST

There are no competing interests.

ORCID

Gunhild Elisabeth Berget  <https://orcid.org/0000-0003-0699-2891>

REFERENCES

- Angulo, J. M., & Madrid, A. E. (2010). Structural analysis of spatio-temporal threshold exceedances. *Environmetrics*, 21, 415–438.
- Azzimonti, D., Bect, J., Chevalier, C., & Ginsbourger, D. (2016). Quantifying uncertainties on excursion sets under a Gaussian random field prior. *SIAM/ASA Journal on Uncertainty Quantification*, 4(1), 850–874.
- Bect, J., Ginsbourger, D., Li, L., Picheny, V., & Vazquez, E. (2012). Sequential design of computer experiments for the estimation of a probability of failure. *Statistics and Computing*, 22(3), 773–793.
- Berget, G. E., Fossum, T. O., Johansen, T. A., Eidsvik, J., & Rajan, K. (2018). Adaptive sampling of ocean processes using an AUV with a Gaussian proxy model. *IFAC-PapersOnLine*, 51(29), 238–243.
- Bhattacharjya, D., Eidsvik, J., & Mukerji, T. (2013). The value of information in portfolio problems with dependent projects. *Decision Analysis*, 10(4), 341–351.
- Bolin, D., & Lindgren, F. (2015). Excursion and contour uncertainty regions for latent Gaussian models. *Journal of the Royal Statistical Society: Series B*, 77(1), 85–106.
- Bolin, D., & Lindgren, F. (2018). Calculating probabilistic excursion sets and related quantities using excursions. *Journal of Statistical Software*, 86(5), 1–20.
- Cetinić, I., Toro-Farmer, G., Ragan, M., Oberg, C., & Jones, B. H. (2009). Calibration procedure for Slocum Glider deployed optical instruments. *Optics Express*, 17(18), 15420–15430.
- Chevalier, C., Bect, J., Ginsbourger, D., Vazquez, E., Picheny, V., & Richet, Y. (2013). Fast parallel kriging-based stepwise uncertainty reduction with application to the identification of an excursion set. *Technometrics*, 56(4), 455–465.
- Cressie, N. A. C., & Wikle, C. K. (2011). *Statistics for spatio-temporal data*. Wiley.
- Eidsvik, J., Mukerji, T., & Bhattacharjya, D. (2015). *Value of information in the earth sciences*. Cambridge University Press.
- Foss, K. H. (2019). *Spatio-temporal Gaussian processes and excursion sets for adaptive environmental sensing using underwater robotics* [Master's thesis]. The Norwegian University of Science and Technology (NTNU).
- Fossum, T. O., Eidsvik, J., Ellingsen, I., Alver, M. O., Fragoso, G. M., Johnsen, G., Mendes, R., Ludvigsen, M., & Rajan, K. (2018). Information-driven robotic sampling in the coastal ocean. *Journal of Field Robotics*, 35(7), 1101–1121.
- Fossum, T. O., Travelletti, C., Eidsvik, J., Ginsbourger, D., & Rajan, K. (2021). Learning excursion sets of vector-valued Gaussian random fields for autonomous ocean sampling. *Annals of Applied Statistics*, 15(2), 597–618.
- French, J. P., & Sain, S. R. (2013). Spatio-temporal exceedance locations and confidence regions. *The Annals of Applied Probability*, 7(3), 1421–1449.
- Gramacy, R. B. (2020). *Surrogates: Gaussian process modeling, design, and optimization for the applied sciences*. Chapman & Hall/CRC Press.
- Rajan, K., & Py, F. (2012). *T-rex: Partitioned inference for AUV mission control*. In *Further advances in unmanned marine vehicles* (pp. 171–199). The Institution of Engineering and Technology.
- Richardson, R. A. (2017). Sparsity in nonlinear dynamic spatiotemporal models using implied advection. *Environmetrics*, 28(6), e2456.
- Rogowski, P., Terrill, E., Otero, M., Hazard, L., & Middleton, W. (2013). Ocean outfall plume characterization using an autonomous underwater vehicle. *Water Science and Technology*, 67(4), 925–933.
- Rye, H., Reed, M., Frost, T. K., Smit, M. G. D., Durgut, I., Johansen, O., & Ditlevsen, M. K. (2008). Development of a numerical model for calculating exposure to toxic and nontoxic stressors in the water column and sediment from drilling discharges. *Integrated Environmental Assessment and Management*, 4(2), 194–203.
- Särkkä, S. (2013). *Bayesian filtering and smoothing*. Cambridge University Press.
- Sigrist, F., Künsch, H. R., & Stahel, W. A. (2015a). spate: An R package for spatio-temporal modeling with a stochastic advection-diffusion process. *Journal of Statistical Software*, 63(14), 1–23.
- Sigrist, F., Künsch, H. R., & Stahel, W. A. (2015b). Stochastic partial differential equation based modelling of large space-time data sets. *Journal of the Royal Statistical Society Series B*, 77(1), 3–33.
- Slagstad, D., & McClimans, T. A. (2005). Modeling the ecosystem dynamics of the Barents Sea including the marginal ice zone: I. Physical and chemical oceanography. *Journal of Marine Systems*, 58(1), 1–18.
- Sommerfeld, M., Sain, S., & Schwartzman, A. (2018). Confidence regions for spatial excursion sets from repeated random field observations, with an application to climate. *Journal of the American Statistical Association*, 113(523), 1327–1340.
- Zhang, S., & Angela, J. Y. (2013). *Forgetful Bayes and myopic planning: Human learning and decision-making in a bandit setting*. In *Advances in neural information processing systems* (pp. 2607–2615). MIT Press.

SUPPORTING INFORMATION

Additional supporting information may be found online in the Supporting Information section at the end of this article.

How to cite this article: Foss, K. H., Berget, G. E., & Eidsvik, J. (2022). Using an autonomous underwater vehicle with onboard stochastic advection-diffusion models to map excursion sets of environmental variables. *Environmetrics*, 33(1), e2702. <https://doi.org/10.1002/env.2702>